New polyvalent low background γ-ray setup at UNamur: Application to S-factor measurements for the 13C(p,γ)14N reaction

Debarsy, Paul-Louis; Baseil, Lucas; Stasser, Coraline; Tabarrant, Tijani; Colaux, Julien; Heuskin, Anne-Catherine; Terwagne, Guy

Published in:
AIP Advances

DOI:
10.1063/5.0178215

Publication date:
2023

Document Version
Publisher's PDF, also known as Version of record

New polyvalent low background γ-rays set-up at UNamur: Application to S-factor measurements for the $^{13}C(p,\gamma)^{14}N$ reaction

P-L Debarsy[1], L. Baseil[1], C. Stasser[1,*], T. Tabarrant[1], J.L. Colaux[1], A-C Heuskin[1], G. Terwagne[1]

[1] LARN, University of Namur, 61 rue de Bruxelles, B-5000 Namur, Belgium

Abstract

The Laboratory of Analysis by Nuclear Reaction (LARN) at the University of Namur (Belgium) is equipped with a low background γ-ray detection system. This setup is made of one ton of lead as passive shielding and plastic scintillators as an anti-cosmic active shielding which covers a large area around a 3.5 × 3.5 inches HPGe detector. This setup makes it possible to reduce the background level from two to three orders of magnitude, depending on the energy range of interest. In this work, this polyvalent detection system is described and used to refine the cross-section measurements of the $^{13}C(p,\gamma)^{14}N$ nuclear reaction at middle and low energies. The reaction $^{13}C(p,\gamma)^{14}N$ plays an important role in the CNO cycle and s-process in stellar evolution. In this work, we studied more precisely the $^{13}C(p,\gamma)^{14}N$ ground transition (E_γ= 8.06 MeV) for incident energies ranging from 147 to 574.3 keV in the centre-of-mass system generated by the 2 MV Tandetron accelerator *ALTAÏS* installed at the LARN. Our measurements performed both in reverse (i.e. $^{1}H(^{13}C,\gamma)^{14}N$) and direct kinematics are in good agreement with all the data available in the literature, validating our low background detection system.

*Corresponding author.
E-mail address: coraline.stasser@unamur.be

1. Introduction

In this work, we present the latest improvements of a polyvalent low background γ-ray detection setup developed at the Laboratory of Analysis by Nuclear Reactions (LARN) at the University of Namur in Belgium. This system can be used for multiple applications: Depth-profiling of light elements (^{1}H, ^{13}C, ^{15}N, ^{19}F for instance), characterization of low-level radioactive samples and cross-section measurements of nuclear reactions.

Measurements of the nuclear cross-section $^{13}C(p,\gamma)^{14}N$ of astrophysical interest [1], both in direct and reverse kinematics, were performed as an application example of such a system. This reaction occurs in the CNO cycle [2, 3] along with the p-p chains [4] and provides the ^{14}N needed to the reaction $^{14}N(p,\gamma)^{15}O$, which is the slowest reaction of the CNO cycle. In addition, the $^{13}C(p,\gamma)^{14}N$ reaction directly competes with the $^{13}C(\alpha,n)^{16}O$ reaction, which is the principal neutron source for the s-process [5]. The $^{13}C(p,\gamma)^{14}N$ reaction presents a resonance at 511 keV (in the centre-of-mass system) for the 8.06 MeV energy level of ^{14}N. This reaction has already been studied in direct [6-10] and reverse [1, 11] kinematics at low energies, providing cross-section values to be compared with our results.

In direct kinematics, it is complicated to produce very low energies close to the Gamow peak (∼100 keV) with a Tandem accelerator. Furthermore, nuclear reactions induced by protons can produce impurities, such as fluor or sodium, acting as a source of noise in the energy region of the gamma rays of interest (∼ 8 MeV). Working in reverse kinematics solves this issue, as the $^{13}C^{+}$ kinetic energy is 1500 keV at the Gamow energy. It however requires producing hydrogen-rich targets, without deuterium. This can be done by ion implantation at low energy with a magnetic deflector, making it possible to separate deuterium from hydrogen. In addition, these targets must stay stable under beam irradiation. This problem was solved by Genard et al. [12] and improved by Debarsy et al. [13].

The first measurements performed with a simplified detection system was carried out by Genard at al. [1], reaching an energy of 225 keV in the centre-of-mass system. The aim of the present paper is to measure the $^{13}C(p,\gamma)^{14}N$ reaction cross-section at lower energies using an improved low background gamma-ray detection system. Measurements in direct kinematics are also presented on a reduced energy region (from 450 to 690 keV in the centre-of-mass system) to evaluate the relevance of the detection setup.

This paper is organized as follows: section 1 describes the low background detection system which is characterized in section 2, while section 3 focuses on an astrophysical application of this setup – i.e. the measurement of cross-section and S-factor values of the $^{13}C(p,\gamma)^{14}N$ reaction.

2. Description of the low background γ-ray detection system

Low-level gamma ray spectroscopy is used for a variety of applications going from radioactive activity analysis [14-20] to low cross-section measurements [21, 22] or material characterization such as elemental depth profiling by resonant nuclear reaction analysis [23].

This kind of spectroscopy requires a setup that mitigates the background level to maximize the signal to noise ratio.

2.1 Source of background in γ-ray spectroscopy

The background comes from three main contributions: natural radioactivity, cosmic rays (mostly muons) and Compton scattering. Natural radioactivity depends on the surrounding materials and is mainly due to three remaining radioactive families (^{235}U, ^{238} U and ^{232}Th) and ^{40}K [15]. The cosmic rays come from the primary flux (mainly protons and helium) interacting with the high atmosphere and producing a secondary flux of particles. At sea level, 75% of these particles are muons with a mean energy of several GeV. Muons can thus deposit a large amount of energy in a γ-ray detector (up to a few tens of MeV, depending on the crystal size and density) [24], which is obviously a source of noise for γ-ray spectroscopy. The last background contribution is due to the Compton inelastic scattering of γ rays inside the detector, leading to a continuum on the left of the photoelectric peak.
There are different ways to mitigate these background sources. For natural radioactivity, it is generally advised to surround the detector by a passive shielding, which consists of high Z materials (e.g. iron or lead) [25]. The shielding thickness depends on the material used. For lead, a thickness from 6 to 10 cm is generally considered. Using a thicker lead shielding is useless because of the interaction of the muons with lead, which leads to additional sources of noise (i.e. Bremsstrahlung and radioisotopes production [25]). One should also carefully choose the detector and shielding materials to avoid any γ-ray emissions from the materials themselves.

Because the muons are very penetrating, a large amount of material (generally expressed in water equivalent depth) is required to significantly reduce their flux. In addition to the muon flux, this amount of material also reduces the neutrons coming from the secondary flux. These neutrons can also provide γ radiation by interacting with the detector or its environment [15]. Some laboratories are installed deep underground to minimize this flux. It is for instance the case of LUNA [26-29], EMMA [30], CASPAR [31] and JUNA [32]. For LUNA, the muon's flux is reduced by about 6 orders of magnitude. In the case of CASPAR, the end station is equipped with a γ-summing spectrometer [33]. Another possibility to mitigate the noise from cosmic rays is to work with an active shielding [34-36], which consists of surrounding the detector with scintillators and performing anticoincidence measurements. This kind of system is much cheaper and easy to develop. However, the neutrons coming from the secondary flux (due to some nuclear reactions in the environment of the detector) and tertiary flux (due to the muon spallation within the passive shielding) can in turn produce radioisotopes, whose disintegration generates γ-rays background [37]. Their contribution depends on the muon and secondary neutron fluxes and the anticoincidence time window when an active shielding is used.

Finally, the Compton scattering background can be mitigated using anticoincidence measurements thanks to an anti-Compton detector added around the γ ray main detector [20, 38-42]. This method is beyond the scope of the present paper as the energy of the detected γ rays is high (8.06 MeV) but is the subject of a future development at the UNamur.

In the case of some cross-section measurements, an extra source of noise can also be produced by the incident beam through parasitic nuclear reactions generated on the beam collimation devices or impurities contained in the target. Working in reverse kinematics while using high-purity targets would greatly help to mitigate this extra source of noise. In the context of the nuclear reaction of interest ($^{13}C(p,\gamma)^{14}N$) studied later in this paper, the signal coming from ^{19}F and ^{23}Na contaminants can be expected in the energy region of interest.

2.2 Low background setup at the LARN

The low background γ-ray detection system developed at the LARN is shown in figure 1. A 3.5 × 3.5 inches High Purity Germanium (HPGe) coaxial detector manufactured by Canberra is used as γ-ray detector. The choice of a HPGe detector makes high precision measurements possible thanks to its high energy resolution (0.3%) compared to other γ-ray detector such as NaI(Tl) (6%) or BGO (12%) [43]. Furthermore, thanks to its important volume, this detector enables high detection efficiency, which is an asset for low counting rate measurements. The relative detection efficiency given by the constructor was 132% at time of purchase.

The passive shielding used to mitigate the natural radioactivity background is presented in figure 2. It is made of 100 mm of low activity lead (i.e. 50 Bq/kg), 20 mm of ultra-low activity lead (i.e. 10 Bq/kg), 2 mm of copper and 4 mm of Plexiglas. The last two layers aim to stop the X-rays produced by the decay chain of ^{210}Pb and slow down the neutrons produced in lead by high energy cosmic rays. During long measurements performed in reverse kinematics, a nitrogen gas flow can be blown around the detector to minimize the radon concentration inside the lead castle [44]. A hole in the lead shielding makes it possible to insert the end of the beam line close to the sample holder, enabling the production of nuclear reactions as close as possible from the detector inside the low background set-up. This hole could be closed thanks to a cap with the same composition as the passive shielding. This configuration enabled radioactive sample analysis for instance. The HPGe detector is placed on a rail which makes it possible to slide it inside the passive shielding. Finally, our laboratory being settled at the ground-floor of a 5-floor building, one can consider that our low background γ-ray acquisition system is located at 6 meters water equivalent (m.w.e.), which reduces the muon flux by 40%.

In addition to the passive shielding, an active shielding was added to mitigate the background caused by cosmic muons inside the germanium crystal. The lead castle is then surrounded by two planar and one hemi-cylindrical plastic scintillators, all EJ-200 manufactured by Scionix, as shown in figure 1. Both planar scintillators are mounted on pistons to raise or lower them when moving the HPGe. Once lowered, the bottom of these scintillators is 2 cm above the bottom of the HPGe detector.

Figure 1: General view of the low background γ-ray detector at the LARN. One can see three plastic scintillators (in black) surrounding the lead castle (in blue). The whole system (i.e. HPGe - lead castle - scintillators) is mounted on a sliding tray which enables to move it close to or away from the end of the beam line.

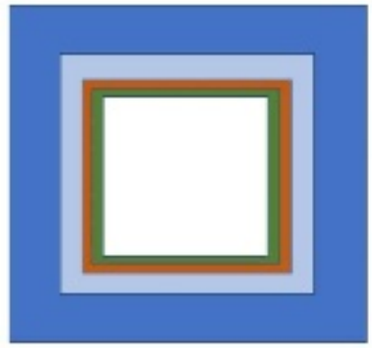

Figure 2: Schematics (not to scale) of the passive shielding of the low background γ-ray detection system at the LARN. The different layers from the outside to the inside are 10 cm of low activity lead (in dark blue), 2 cm of ultra-low activity lead (in light blue), 2 mm of copper (in orange) and 4 mm of Plexiglas (in green). The central cavity where the HPGe can be inserted appears in white.

Thanks to a numerical acquisition system from CAEN [45], it is possible to set up an anticoincidence between the HPGe detector and the plastic scintillators. A Digital Pulse Processing for the Pulse Height Analysis (DPP-PHA) and MC^2 Analyser or CoMPASS software were used to perform the measurements. With this active shielding, we expected a high shielding efficiency against cosmic rays since the muons have a $\cos^2(\theta)$ distribution (with θ = 0° at the zenith) [46]. Note that, to evaluate the efficiency of our active shielding, we split the output signal from the pre-amplifier of the HPGe and thus simultaneously recorded the spectra with and without the veto.

2.3 Characterization of the setup

Figure 3 shows the background subtraction efficiency of the low background γ-ray detector used for this work. One can see that the passive shielding already reduces the γ-ray background by more than 2 orders of magnitude, depending on the energy region. Some peaks, present as contaminants in materials or air around the HPGe detector, or in the components of the detector itself, are still present, such as the ^{40}K at 1460.8 keV, the ^{222}Rn at 1764.5 keV, ^{208}Tl (^{232}Th family) at 2614 keV, as well as the annihilation peak at 511 keV. The high intensity of the annihilation peak is due to photons coming from e^+ - e^- annihilations induced by bremsstrahlung radiations of muons interacting within the lead castle [47]. Turning ON the active shielding further reduces the γ-ray background up to one more order of magnitude for energies above 3 MeV.

Figure 4 shows spectra similar to those in figure 3, except that the energy range is respectively from 0 to 12 MeV at high resolution (figure 4a) and 0 to 67 MeV at low resolution (figure 4b). Figure 4 shows the typical muon spectrum expected for such experimental conditions. Below 7 MeV, the spectrum is dominated by indirect muon interactions in the lead shielding [48, 49]. Above 7 MeV, the spectrum is dominated by direct muon interaction in the Ge crystal [48, 49]. Figure 4b highlights a broad peak observed around 60 MeV, which is ascribed to the direct interaction of muons with the HPGe detector [24, 48]. Indeed, the muon energy loss into germanium is about 7.3 MeV.cm^{-1} [24, 48] and the thickness of our HPGe is 86 mm. We can therefore expect an energy peak around 60 MeV. The width of this peak is related to the muon path in the HPGe detector. Due to the angular distribution of muons, it is indeed more likely that muons reach the crystal from the zenith, crossing all the width of the crystal, giving rise to the maximum of the peak. A weaker part of the muons can take smaller or larger paths in the crystal. This peak disappears when the active shielding is turned ON.

One can conclude that the present setup makes it possible to decrease the noise by one order of magnitude between 3-7 MeV and by two orders of magnitude above 8 MeV.

In addition to figures 3 and 4, table 1 summarizes the detection rates (with background correction) of characteristic γ peaks and two energy regions for external (i.e. no shielding), internal without veto (i.e. passive shielding) and internal with veto (i.e. passive and active shielding) acquisition conditions. The “ratio” values give the internal (with or without veto) detection rate over the external detection rate. One can see that the passive shielding makes it possible to mitigate 98% of the background between 0.3 and 3 MeV. The mitigation of the muon background is about 95% between 3 and 66 MeV. Due to the absence of natural radioactivity beyond 3 MeV, this result corroborates the really good efficiency of the active veto. The background reduction is weaker at lower energy (54%). This difference in the efficiency of the active veto in function of the energy is explained by the indirect (below 7 MeV) and direct (above 7 MeV) nature of muon interactions in the Ge crystal.

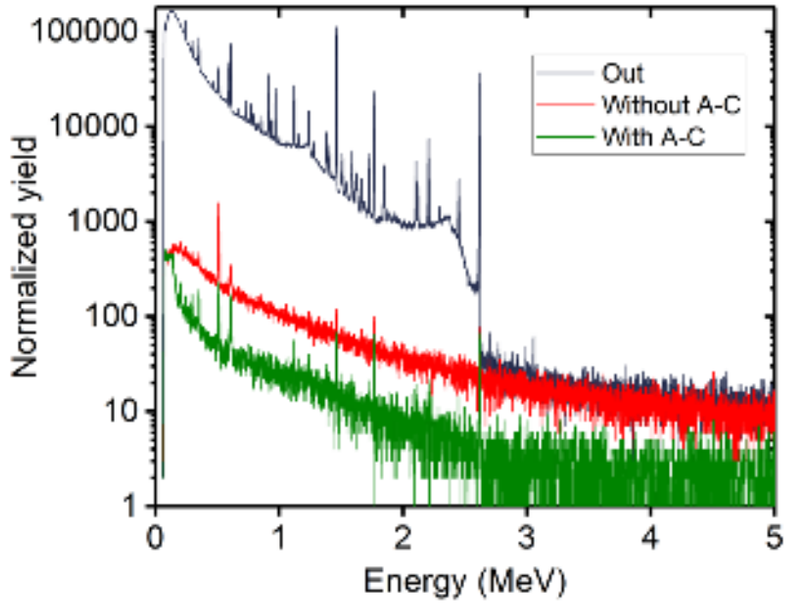

Figure 3: HPGe spectra of natural radioactivity outside the lead castle (in dark blue), inside the lead castle without active veto (in red) and inside the lead castle with active veto (in green). All spectra are normalized by the acquisition time.

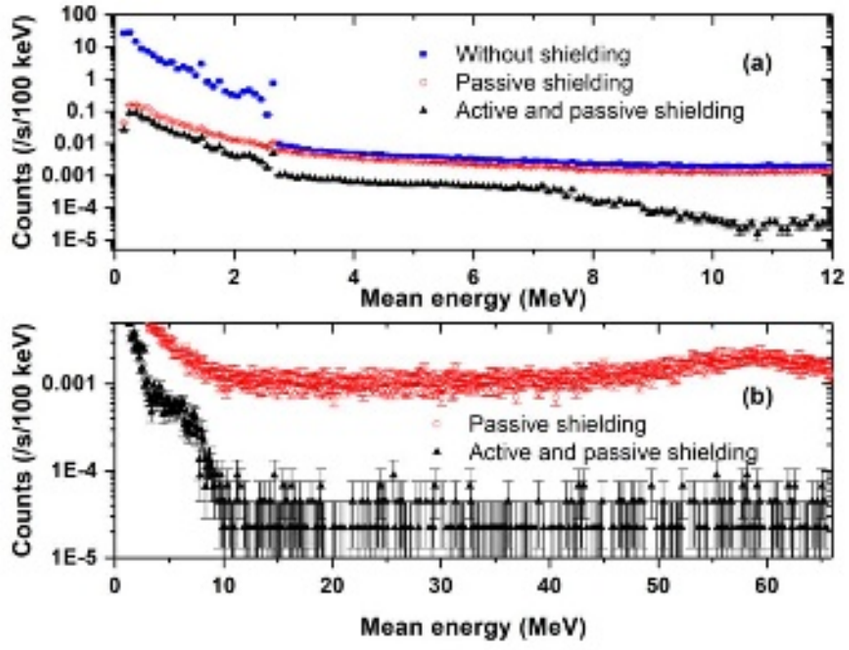

Figure 4: Counting rate (/s/100 keV) in the HPGe detector for different energy regions and for different configurations of the detection setup. (a) HPGe detector outside passive shielding (blue squares), inside passive shielding (red circles) and inside the passive shielding with veto activated (black triangles) for an energy range from 0 to 12 MeV. (b) HPGe detector outside passive shielding (red circles) and inside passive shielding with veto activated (black triangles) for an energy range from 0 to 65 MeV. Uncertainties are calculated at 98% C.L.

It is also noteworthy that for the 609.3 keV, 1460.8 keV and 2614.6 keV peaks, the values for the configurations with or without veto are very close to each other considering the error bars (mainly dominated by the counting statistics for the 609.3 keV peak). This means that the number of accidental anticoincidence is low and therefore validates our active shielding configuration. Concerning the annihilation peak at 511 keV, it is consistent that the ratio decreases when the active shielding is activated since this peak is partly due to the muons generating electron-hole pairs within the materials surrounding the detector (mainly the lead castle). It is finally important to notice that we did not observe γ rays coming from neutron inelastic scattering on ^{74}Ge (596 keV) and ^{72}Ge (693 keV) [50]. While this background contribution becomes significant in the context of ultra-low background experiment, it is negligible compared to the background detection rate in our setup.

It is also under interest to highlight that this low background setup makes it possible to reach a minimum detectable activity around 0.1 Bq for ^{137}Cs and ^{60}Co for a point-like sample located in the lead chamber at 3 mm in the front of the HPGe detector and for less than 5 hours of acquisition.

Table 1: Comparison of detection rates (counts per hour) for several γ peaks or energy regions for external (outside lead castle), internal (inside lead castle) without veto and internal with veto acquisitions. Acquisition times are 63 hours for external conditions and 48 hours for internal conditions. Uncertainties are calculated at 68% C.L.

Energy (MeV)	***0.511***	***0.609***	***1.460***	***2.614***	***0.3 - 3***	***3 - 66***
Family	Annihilation peak	^{214}Bi (^{238}U)	^{40}K	^{208}Tl (^{232}Th)		
External	1437.5 ± 4.8	3781.0± 7.7	1464.8± 4.8	2572.8± 6.4	$2.28\ 10^{5}$	$3.88\ 10^{3}$
Passive shielding	91.7 ± 14	2.0 ± 0.2	4.2 ± 0.2	3.2 ± 0.2	$3.73\ 10^{3}$	$3.25\ 10^{3}$
Ratio to external	$(64 \pm 2)\ 10^{-3}$	$(5.3\pm0.5)\ 10^{-4}$	$(2.9\pm0.2)\ 10^{-3}$	$(1.2\pm0.1)\ 10^{-3}$	$1.6\ 10^{-2}$	$8.4\ 10^{-1}$
Active shielding	14.1 ± 0.5	1.6± 0.2	4.4± 0.3	3.1± 0.2	$1.72\ 10^{3}$	$1.32\ 10^{2}$
Ratio to passive shielding	$(1.5 \pm 0.2)\ 10^{-1}$	$(8\pm0.1)\ 10^{-1}$	(1.0 ± 0.1)	$(9.7\pm0.1)\ 10^{-1}$	$4.6\ 10^{-1}$	$4.1\ 10^{-2}$

Finally, we compared our setup to other facilities. Table 2 shows the counting rate by kilogram of detector and by minute of acquisition for different facilities in their experimental conditions (depth and veto form). At energies below 3 MeV, we found that our system is competitive compared to other systems under similar conditions (i.e. from ground level to maximum 10 m.w.e. underground facilities). For instance, we obtained similar detection rates, even better than those measured by Laurec et al. [51], Shizuma et al. [50] and J.I. Byun et al. [18]. This first result is not very surprising because these facilities have an active shielding similar to the one used on our device (almost a 4π shielding). However, these facilities are a bit more complex than our setup. For example, in the case of Gastrich et al. [15], their system lies in a steel box surrounding the whole laboratory, which enables the absorption of a part of the cosmic rays. In the case of Sivers et al. [52], in addition to their 4π active shielding, the passive shielding is placed into a hermetic box to limit radon contamination. The system of PRISNA [53] is the closest to ours. Indeed, their facility consists in five plastic scintillators covering all the passive shielding, except the bottom. The passive shielding is made of 10 cm of lead, following by 8 cm of borated polyethylene and 4 cm of archaeological lead. The whole laboratory is in a hermetic room to avoid radon contamination. Concerning GIOVE, from Heusser et al. [54], this system is more efficient than ours. In addition to being located at 15 m.w.e. underground, their facility is characterized by an active shielding inside and outside the passive shielding. Moreover, the passive shielding is made of different layers of lead and borated polyethylene to suppress respectively γ ray and neutron background. For facilities deeper underground (> 33 m.w.e.), the detection rates are about one to two orders of magnitude lower than ours. As we can see in the table 2, these laboratories do not need an active shielding [54-56]. The system of S. Turkat et al. [57] achieves a very low counting rate comparable to facilities located deeper underground. This system is close to our device but is located deeper underground (140 m.w.e.) and made of a thicker passive shielding and an anti-radon box. One can conclude that our system is totally suitable for applications associated with low counting rates, such as elemental depth profiling, characterization of radioactive wastes or low cross-section measurements. When ultra-low background measurements are required (e.g. activity measurements of a few tens of μB/kg), systems such as Heusser and al. [54], S. Turkat et al. [57] or systems located deep underground would be more efficient. However, these kinds of facilities are expensive.

Now looking at the energy range above 3 MeV, one can see that the detection rate is systematically lower than other facilities. However, data above 3 MeV in literature are sparse, so we can only refer to a small number of facilities. In the case of Kasperovych et al. [36], they did not use an HPGe detector, but a CdWO4. Longland et al. [21] have a detection rate close to ours. In their case, they used an active shielding surrounding the detector inside the passive shielding. However, in addition to this active shielding, they also performed γγ-coincidences which are not considered in table 2. If this coincidence is activated, their detection rate falls to 0.29 min^{-1} kg^{-1}. Finally, one can notice that our detection rate is about three times lower than the counting rate obtained by Genard et al. [1 , 58], the previous detection device used at the LARN. This improvement is explained by the increase in solid angle of the active shielding.

Table 2: Comparison of the shielding efficiency (in kg^{-1} min^{-1}) as a function of the energy range for different low background facilities. A part of these results comes from [15, 59]. For each facility, the depth in m.w.e. as well as the form of the active shielding are given. The results coming from this work were performed in our experimental conditions – i.e. a hemi-cylindrical and two plan plastic scintillators as active shielding and at a depth of 6 m.w.e.

	Other facilities				**This work (6 m.w.e.)**
gy region (keV)	Active shielding	Depth (in m.w.e.)	References	Counting rate (kg^{-1} min^{-1})	Counting rate (kg^{-1} min^{-1})
0-2000	1 plastic sc.	Ground level	*Miley et al. [60]*	4.63	4.75
0-2400	1 plastic sc.	Ground level	*N. Q. Hung et al. [19]*	111.35	6.41
7-2700	5 plastic sc.	6 m.w.e	*Prisna [53]*	8.87	6.65
0-2700	6 plastic sc.	Ground level	*Laurec et al. [51]*	9.81	6.52
0-2700	6 plastic sc.	1 m.w.e.	*Schwaiger et al. [61]*	5.69	6.18
0-2700	4 plastic sc.	10 m.w.e.	*Gastrich et al. [15]*	2.53	6.18
0-2700	7 external plastic sc. and 6 internal plastic sc.	15 m.w.e.	*Heusser et al. [54]*	0.24	6.18
0-2700	5 plastic sc.	140 m.w.e	*S. Turkat et al. [57]*	0.08	6.18
0-2700	/	500 m.w.e.	*Koehler et al. [55]*	0.17	6.18
0-2700	/	3800 m.w.e.	*Heusser et al. [54]*	0.05	6.18
0-2700	/	4800 m.w.e.	*Reyss et al. [56]*	0.13	6.18
0-2700	1 plastic sc.	≤ 33 m.w.e.	*Semkow et al. [59]*	7.66	5.89
0-2700	6 plastic sc.	10 m.w.e.	*Sivers et al. [52]*	1.20	5.05
0-3000	4 internal plastic sc.	Ground level	*Shizuma et al. [50]*	15.80	6.23
0-3000	5 plastic sc.	Ground level	*J. I. Byun et al. [18]*	13.86	6.23
00-5000	1 plastic sc.	Ground level	*Kasperovych et al. [36]*	0.41	0.31
00-9000	5 plastic sc.	Ground level	*Longland et al. [21]*	1.00	0.62
00-9000	1 plastic sc.	6 m.w.e.	*Genard et al. [1]*	1.60	0.62

3. Astrophysical application

In nuclear astrophysics, values of cross-sections are required to obtain the rates of nuclear reactions in stars [4], which enables one to make predictions about star evolution. The reaction rate of stellar reactions is maximum in the "Gamow window", which arises from the convolution of the Maxwell-Boltzmann energy distribution of particles in the star and the tunnelling probability between the interacting nuclei. This peak appears in an energy range around few tens of keV (84.7 keV for the ^{13}C(p,γ)^{14}N reaction). Therefore, since the cross-section decreases with the incident energy, the measurements around the Gamow window require a very long acquisition time for which handling the background noise becomes a major concern. Accurate measurements at those energies require a low background setup. Even though, it is not always possible to obtain cross-section values at Gamow energies and the astrophysicists generally rely on the extrapolation of their data. To do this, they use the S factor which is defined as follows:

$$S(E) = \sigma(E) E \exp(2\pi\eta)\,, \quad (1)$$

where $\sigma(E)$ is the cross-section, E the energy in the centre-of-mass and η the Sommerfeld parameter. In numerical units, the exponent can be expressed as [4]:

$$2\pi\eta = 31.29 Z_1 Z_2 \left(\frac{\mu}{E}\right)^{1/2}, \quad (2)$$

with Z_1 and Z_2 the atomic numbers of the colliding nuclei, μ the reduced mass (in amu) and E the centre-of-mass energy in keV. It should be noted that the S-factor varies significantly less than the cross-section with the incident energy, which makes it easier to extrapolate to low energies [4].

3.1 Experimental procedure

Considering the ^{13}C(p,γ)^{14}N nuclear reaction, the number N_γ of detected events for a specific γ-ray transition is given by:

$$N_\gamma = N_i\,[C_x]\,f_b\,\Omega\,\varepsilon(E)\,\frac{d\sigma(E)}{d\Omega}\,, \quad (3)$$

where N_i is the number of incident ions, $[C_x]$ the concentration of the element C within the target, f_b the branching ratio of the specific transition, Ω is the solid angle of detection, $\varepsilon(E)$ the detection efficiency and $\frac{d\sigma(E)}{d\Omega}$ is the differential cross-section. This equation highlights that four parameters can be tuned to maximize the detection rate, namely:

- the beam intensity, related to the ion beam source and the beam transmission through the beamline;
- the target composition, tuneable through the target synthesis process;
- the detection efficiency;
- and the solid angle of detection.

These four parameters will be discussed in the following sections.

We measured the cross-section of the $^{13}C(p,\gamma)^{14}N$ reaction by detecting the 8.06 MeV γ coming from the resonant level (1^-) to the ground state (1^+). This is a E_1 transition which is isotropic, therefore, we did not have to deal with angular dependence. As we considered only this transition, we first determined its branching ratio by setting the beam energy to the resonance and taking a long acquisition. We found a normalization factor f_b of 1.25, which is in agreement with literature [6, 62]. For γ-ray detection, we selected the full energy peak region as a region of interest (ROI) for two reasons:

- the signal-to-noise ratio is greater in this ROI than in the one including the first and second escape peaks,
- the detection efficiency is easier to determine for a single energy than for a wide energy range.

As a result of this choice, the counting rate is reduced.

3.2 Experimental setup

3.2.1 Ion beam source and beam line description

The beam intensity relies mainly on the accelerator performance. In our case, we used the 2 MV Tandetron accelerator *ALTAÏS* which is equipped with a Negative Ions Source (SNICs) capable of delivering beam intensities of a few µA on the target for acceleration voltages ranging from 150 to 2000 kV.

To keep high beam intensities at low energy in the centre of mass system, it is suitable to work in reverse kinematics. Our Tandetron accelerator is indeed better suited for working with medium energy carbon beams (~1400 keV) rather than very low energy proton beams (~100 keV). In addition, all collimation devices (slits and collimators) are plated with gold (collimators) or tungsten (slits). It is noteworthy that working in reverse kinematic requires longer acquisition time than direct kinematic, since ^{13}C targets can reach higher concentration than ^{1}H targets (see next section).

A new beam line was designed as shown in figure 5. The LN2 cold trap is about 30 cm long and stops at about 5 cm from the sample. It is streaked on its inner face to reduce the carbon build-up occurring during long data acquisitions and to improve its pumping efficiency. Regarding the collected charge determination, we added two permanent magnets (NdFeB, 10 mm diameter, 20 mm height from *supermagnete*) and applied a voltage of -300 V on the LN2 cold trap to prevent secondary electrons from escaping the sample under irradiation. To validate the current integration, a *PIPS* detector was set around 176° (relative to the incident beam direction) at a distance giving a solid angle of detection equal to $(9.98 \pm 0.11) \times 10^{-2}$ msr. The spot size was set to about 1 cm² using square slits. The HPGe detector was aligned with the beam line direction and the distance between its endcap and the outer surface of the sample holder is 3 mm. In these experimental conditions, the solid angle of detection is 1.36 ± 0.04 sr.

For the measurements performed in reverse kinematics, the sample holder was cooled by Syltherm to limit the heating of the sample under irradiation. The sample was also mounted on a carbon sheet to ensure a good thermal contact with the sample holder.

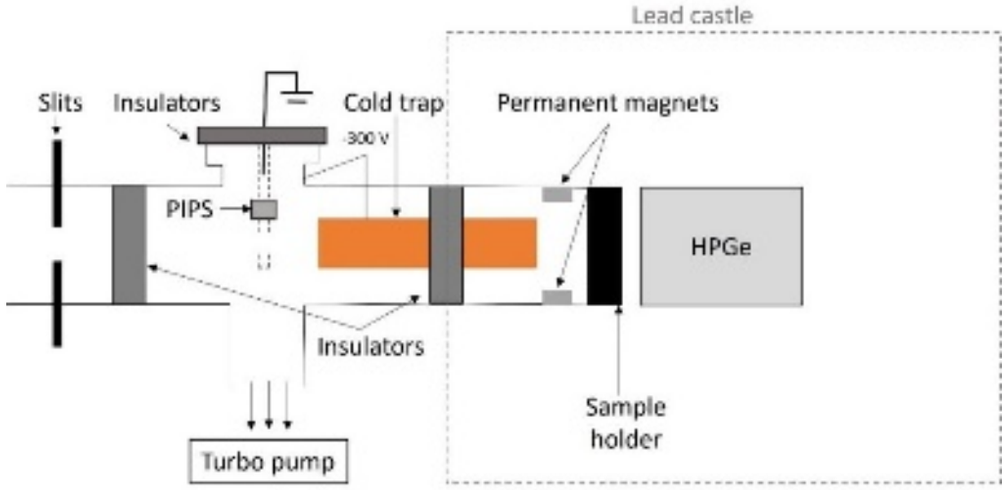

Figure 5: Sketch of the end-station used in this work.

3.2.2 Target description

Measuring the cross-section of the $^{13}C(p,\gamma)^{14}N$ reaction requires to use targets that are (i) stable under beam irradiation, (ii) have a high hydrogen or carbon concentration and (iii) have no impurities (especially no ^{2}H for ^{1}H targets). In this work, we chose to use solid targets that meet all those requirements.

The synthesis of the hydrogen solid targets was carried out by implanting 5 keV $^{1}H^{+}$ in amorphized silicon layer of about 300 nm thick with an implanted dose of 3×10^{17} at.cm^{-2}. All the details about the synthesis and characterization of those hydrogen targets are presented in reference [13], but briefly:

a) Isotopic purity of the $^{1}H^{+}$ implantation beam was ensured using a 90° magnetic deflection. The implantation was carried out with the duoplasmotron source installed on ALTAÏS and the Si target was placed on the hole beside the Low Energy Faraday cup.
b) The use of amorphized silicon layer made it possible to increase the retained ^{1}H dose by a factor 2.6 compared to an equivalent implantation performed in crystalline silicon [12].

We finally obtained solid targets containing about 30 atomic percent of ^{1}H with a retained dose around 2.4×10^{17} at.cm^{-2}. However, even though it decreased rapidly with irradiation time, we should highlight that the ^{2}H contamination coming from water surface absorption could not be avoided. It is also noteworthy that using $K^{13}C^{15}N$ powder in the SNICs source enabled us to easily switch from a ^{13}C beam for cross-section measurements to a ^{15}N beam for checking the target stability by depth profiling the hydrogen with the $^{1}H(^{15}N,\alpha\gamma)^{12}C$ nuclear reaction that presents a strong and narrow resonance at 6385 keV [63].

For measurements carried out in direct kinematics, ^{13}C targets were synthesized by 36 keV $^{13}C^-$ ion implantation into amorphized silicon with the same system as explain above for $^1H^+$ implantation using the injector of the accelerator as an implanter. The nominal dose was 10^{18} at/cm^2. The retained dose was measured to be 9.96×10^{17} at.cm^{-2}. Details about the synthesis and characterization of those ^{13}C targets will be presented in an upcoming paper.

3.2.3 Beam line characterization and detection efficiency

The beam current integration was carried out with an Ortec 429 module which has been proven to be accurate at 3% using the backscattered particles yield measured by the PIPS detector.

The use of the cold finger greatly reduces the carbon build-up on the target during the measurements. For example, the energy lost by 2170 keV ^{13}C within the carbon build-up layer after 7 hours irradiation with 2 µA was about 10 keV, for a pressure around 2.5 10^{-7} mbar. Note that this is highly dependent of the partial pressure in the close vicinity of the target. This energy loss can reach 50 keV for similar beam conditions at a pressure of 5.6 10^{-7} mbar.

The detection efficiency with respect to the γ-ray energy was calculated using the version 10.1 of the Geant4 toolkit, an open-source code [64], more precisely using the Low energy Livermore physics list. A sketch of the experimental geometry modelled in Geant4 is shown in figure 6.

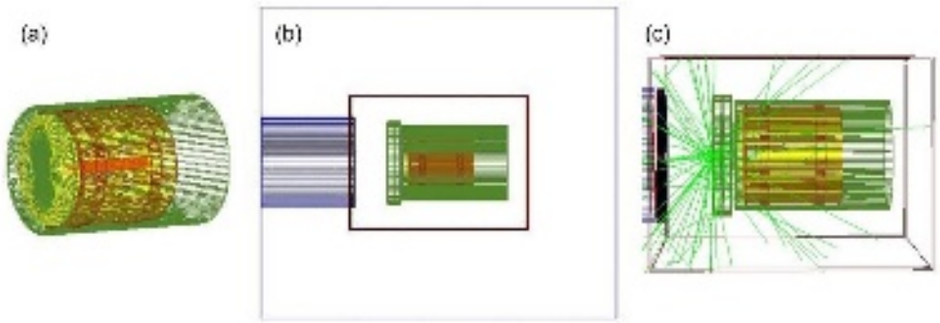

Figure 6: Geant4 modelling of the experimental detection setup. The different components are: lead (dark blue), copper (red), Plexiglas (in dark), stainless steel (in dark green), germanium (in yellow). (a) Modelling of the HPGe detector characterized by a germanium crystal of 86 x 88 mm^2. (b) Modelling of the HPGe detector in the detection chamber embedded in the passive shielding made of lead, copper and Plexiglas. (c) Position of the isotropic source placed at the same position as the sample in a sample holder with gamma rays appearing in light green. The distance between the sample holder and the endcap of the HPGe detector is 3 mm and the total distance between the endcap of the detector and the surface of the sample is 20 mm.

The detection efficiency was numerically calculated for different energies using an isotropic source of the same size as the beam spot on the target. Numerical results were compared to experimental measurements carried out with ^{137}Cs (40.7 kBq), ^{60}Co (0.261 MBq), ^{152}Eu (2.20 kBq), ^{133}Ba (23.37 kBq) and ^{141}Am (0.380 MBq) radioactive sources placed in the same position

as the sample. In order to compare the simulated results to experimental measurements at higher energy, we used the γ ray of 8.06 MeV emitted by the $^{13}C(p,\gamma)^{14}N$ reaction which presents a resonance at 511 keV in the centre-of-mass system. The value of the cross-section being well known at this energy, and in agreement between all authors [1, 65], one can use this reaction to derive the detection efficiency thanks to equation (3). This measurement of the efficiency at the energy of interest made it possible to consider the drop in the HPGe detection efficiency over time. Figure 7 shows the simulated and experimental detection efficiency of the HPGe detector as a function of γ-ray energy. Each simulated point was obtained by sending 10^6 photons. The error bar for the experimental efficiency at 8.06 MeV is related to errors on ^{13}C concentration (~8 %), current integration (~3 %) and counting statistics (<1 %) as well as uncertainties on the reaction cross-section (~10%) and branching ratio (< 1 %). One can see that simulated and experimental results are in close agreement above 300 keV. At lower energy, there is an important discrepancy, related to the poor knowledge of the HPGe geometry (mainly the dead layer) and the components and dimensions of the sample holder. As shown in figure 7, a polynomial function of degree 8 is fitted through the simulated data.

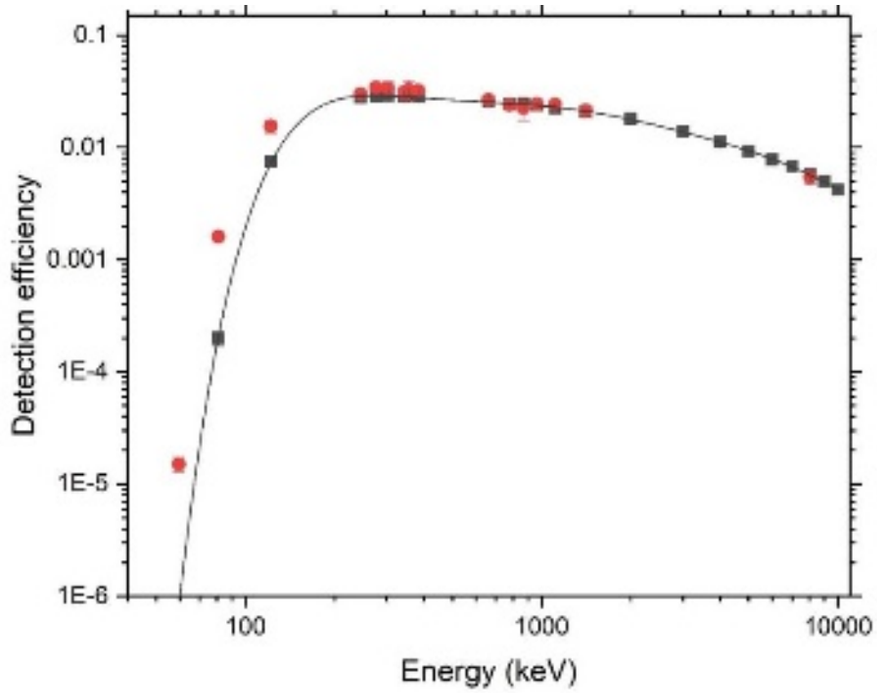

Figure 7: Measured (red dots) and simulated (black squares) absolute detection efficiency of the HPGe detector with respect to the photon energy in experimental conditions. The experimental data was obtained thanks to ^{137}Cs, ^{60}Co, ^{152}Eu, ^{133}Ba and ^{141}Am radioactive sources placed inside the sample holder. A polynomial function is fitted in the simulated data. Experimental errors consider the statistical errors and uncertainties on branching ratios and source activities. For the experimental efficiency at 8.06 MeV, the error is mainly due to the cross-section, ^{13}C concentration and current reading uncertainties.

For the energy under interest (i.e. 8.06 MeV), we obtained a detection efficiency of 5.575×10^{-3}, which is actually a mean value between the experimental detection efficiency measured with the $^{13}C(p,\gamma)^{14}N$ reaction and the simulated value, both represented in figure 7.

3.3 Results and discussions

In this work, we measured the cross-section of the $^{13}C(p,\gamma)^{14}N$ reaction respectively from 512 to 147 keV in the centre-of-mass system (with energy correction) in reverse kinematic and from 628.6 to 397.1 keV in direct kinematic.

Measurements in direct and reverse kinematics were plotted on figure *8* with data from *Genard et al. [1],* King *et al. [6]* and *Vogl* [65]. The S-factor is also represented. Vertical error bars are related to the following contributions: the statistical errors, the hydrogen/carbon concentration, the detection efficiency, and the current integration uncertainties. The horizontal error bars are related to the beam energy uncertainty. Note that the average beam energy was calculated as the incident energy lowered by half the beam energy loss in the target, typically 70 keV, and the carbon build-up layer, typically 30 keV in reverse kinematics. The uncertainty on the energy was estimated to 3%, considering the error on the accelerator calibration, the uncertainty on the stopping power and the energy lost by incident particles when passing through the stripper channel of the accelerator. The latter depends on the pressure inside the channel which was estimated on the basis of available data [66].

Looking at figure 8, one can observe that the results are in good agreement with other references. Indeed, one can notice that the intensity and the width of the resonance at 511 keV are in agreement with all available data.

King *et al.* used two accelerators to obtain all their measurements. In our case, we used a single accelerator, which is not dedicated to astrophysical applications (for example, our beam intensities were around few µA against several hundred µA in the case of King). In the case of Vogl, he switched his proton beam to dihydrogen beam to keep high current at low energies. Deuterium cannot be separated from dihydrogen by a magnetic selector, which had as consequences to send deuterium on the target and produce background.

Tables 3 et 4 give cross-section and S-factor values respectively in reverse and direct kinematics.

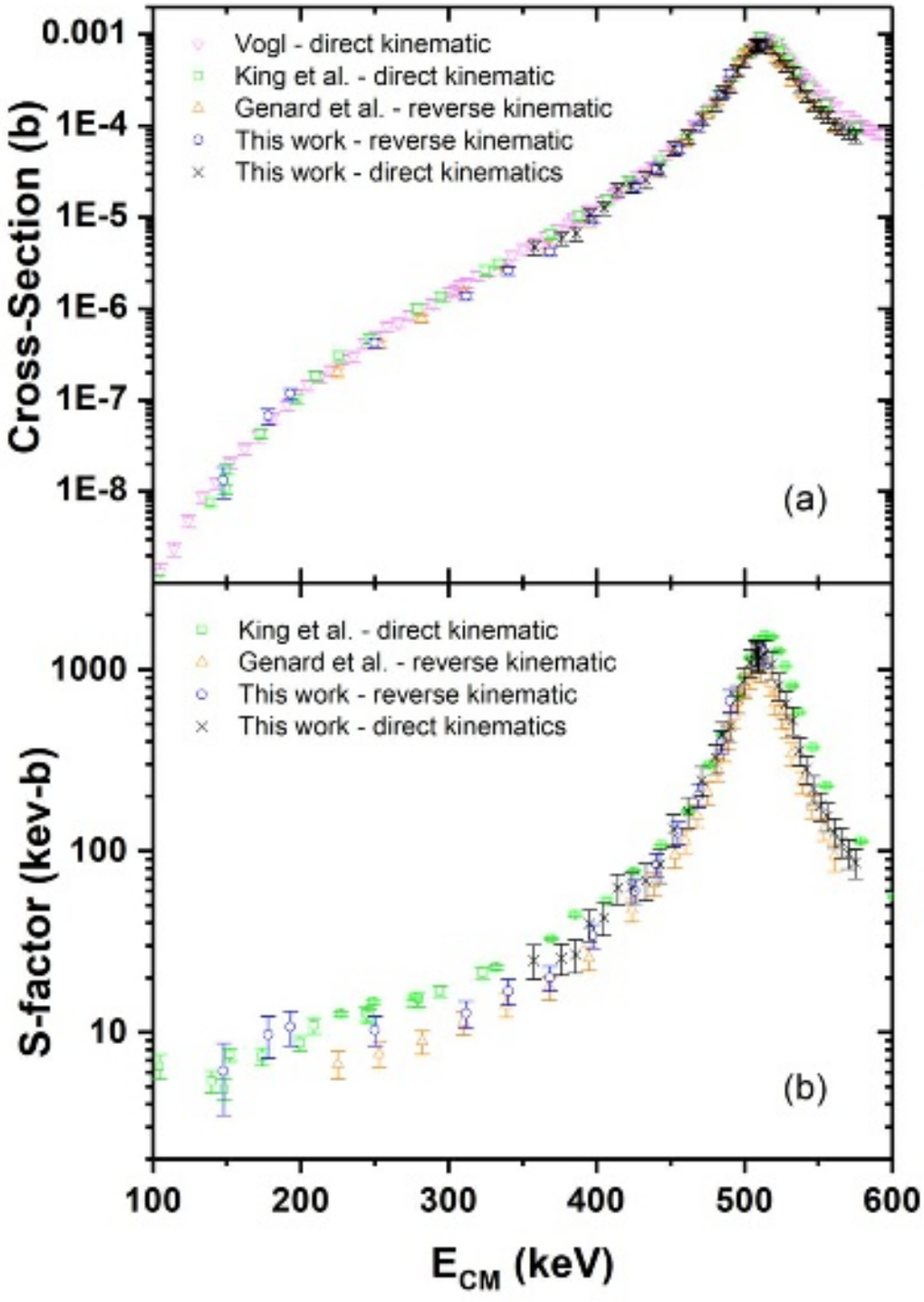

Figure 8: Cross-section (a) and S-factor (b) measurements of the $^{13}C(p,\gamma)^{14}N$ reaction. Our results in reverse and direct kinematics (blue circles and black crosses) are compared to those of Genard et al. (orange triangles), King et al. (green squares) and Vogl (red triangles). Error bars on the S-factor are related to statistical errors, errors on the current and the thickness of the implanted region.

Table 3: Overview of the results in reverse kinematics for the transition coming from the resonant level (1^-) to the ground state of the $^{13}C(p,\gamma)^{14}N$ reaction.

E_{lab} keV)	E_{CM} (keV)	E_{CM} Error (keV)	Cross-section (b)	Absolute error (b)	Relative error (%)	S-factor (keV.b)	Absolute error (keV b)	Relative error (%)
7200	512.3	15.4	8.04E-04	8.7E-05	10.8	1.26E+03	1.8E+02	14.1
6900	490.2	14.7	3.77E-04	4.1E-05	10.8	6.74E+02	9.6E+01	14.2
6800	484.4	14.5	2.17E-04	2.3E-05	10.8	4.02E+02	5.7E+01	14.3
6600	469.1	14.1	9.83E-05	1.1E-05	10.7	2.02E+02	2.9E+01	14.4
6400	455.1	13.7	5.55E-05	5.9E-06	10.7	1.26E+02	1.8E+01	14.5
6200	440.7	13.2	3.35E-05	3.6E-06	10.7	8.43E+01	1.2E+01	14.6
6000	425.9	12.8	2.12E-05	2.3E-06	10.8	5.98E+01	8.9E+00	14.8
5800	397.5	11.9	9.48E-06	1.0E-06	10.7	3.40E+01	5.1E+00	15.1
5600	368.4	11.1	4.22E-06	4.5E-07	10.8	2.00E+01	3.1E+00	15.5
5400	340.3	10.2	2.62E-06	2.8E-07	10.8	1.68E+01	2.7E+00	15.9
5200	311.5	9.3	1.39E-06	1.5E-07	10.8	1.27E+01	2.1E+00	16.4
4600	250.0	7.5	4.26E-07	4.8E-08	11.2	1.03E+01	1.9E+00	18.1
4300	193.1	5.8	1.17E-07	1.6E-08	13.5	1.07E+01	2.3E+00	21.4
4188	177.9	5.3	6.66E-08	1.3E-08	19.0	9.69E+00	2.5E+00	25.8
4160	147.8	4.4	1.34E-08	5.0E-09	37.4	6.09E+00	2.6E+00	42.1

Table 4: Overview of the results in direct kinematics for the transition coming from the resonant level (1^-) to the ground state of the $^{13}C(p,\gamma)^{14}N$ reaction.

E_{lab} keV)	E_{CM} (keV)	E_{CM} Error (keV)	Cross-section (b)	Absolute error (b)	Relative error (%)	S-factor (keV.b)	Absolute error (keV b)	Relative error (%)
628,6	575,0	17,3	7,71E-5	1,28E-5	16,6	8,61E+1	1,60E+1	18,6
623,6	570,3	17,1	8,47E-5	1,39E-5	16,4	9,69E+1	1,78E+1	18,4
618,6	565,6	17,0	9,53E-5	1,54E-5	16,2	1,12E+2	2,04E+1	18,2
613,5	560,9	16,8	1,06E-4	1,69E-5	16,0	1,27E+2	2,30E+1	18,1
608,5	556,2	16,7	1,26E-4	1,98E-5	15,7	1,55E+2	2,77E+1	17,8
603,5	551,4	16,5	1,41E-4	2,18E-5	15,5	1,77E+2	3,14E+1	17,8
598,4	546,7	16,4	1,70E-4	2,60E-5	15,3	2,19E+2	3,85E+1	17,6
593,4	542,0	16,3	2,14E-4	3,22E-5	15,1	2,82E+2	4,92E+1	17,4
588,3	537,3	16,1	2,63E-4	3,92E-5	14,9	3,57E+2	6,16E+1	17,3
583,3	532,6	16,0	3,78E-4	5,54E-5	14,7	5,25E+2	8,99E+1	17,1
578,3	527,9	15,8	4,51E-4	6,58E-5	14,6	6,45E+2	1,10E+2	17,1
573,2	523,1	15,7	5,53E-4	8,01E-5	14,5	8,11E+2	1,38E+2	17,0
568,2	518,4	15,6	7,08E-4	1,02E-4	14,4	1,07E+3	1,81E+2	17,0
563,2	513,7	15,4	7,96E-4	1,15E-4	14,4	1,23E+3	2,09E+2	17,0
558,9	509,7	15,3	7,29E-4	1,03E-4	14,1	1,16E+3	1,94E+2	16,8
558,1	509,0	15,3	7,48E-4	1,08E-4	14,4	1,19E+3	2,03E+2	17,0
558,1	509,0	15,3	7,82E-4	1,13E-4	14,4	1,25E+3	2,12E+2	17,0
556,7	507,7	15,2	7,68E-4	1,10E-4	14,3	1,23E+3	2,09E+2	16,9
553,1	504,2	15,1	6,66E-4	9,62E-5	14,4	1,09E+3	1,87E+2	17,1
548,0	499,5	15,0	5,17E-4	7,51E-5	14,5	8,72E+2	1,50E+2	17,2
543,0	494,8	14,8	3,99E-4	5,84E-5	14,6	6,92E+2	1,20E+2	17,3

538,0	490,1	14,7	2,71E-4	4,03E-5	14,9	4,85E+2	8,51E+1	17,5
532,9	485,4	14,6	2,36E-4	3,53E-5	15,0	4,35E+2	7,68E+1	17,7
527,9	480,6	14,4	1,71E-4	2,61E-5	15,3	3,24E+2	5,82E+1	18,0
517,8	471,2	14,1	1,21E-4	1,91E-5	15,7	2,45E+2	4,52E+1	18,4
507,7	461,7	13,9	7,65E-5	1,27E-5	16,6	1,65E+2	3,18E+1	19,2
497,7	452,3	13,6	5,71E-5	9,92E-6	17,4	1,32E+2	2,63E+1	19,9
487,6	442,8	13,3	3,41E-5	6,58E-6	19,3	8,45E+1	1,83E+1	21,7
477,5	433,4	13,0	2,59E-5	5,35E-6	20,7	6,89E+1	1,59E+1	23,0
467,4	423,9	12,7	2,21E-5	3,60E-6	16,3	6,33E+1	1,22E+1	19,3
457,4	414,4	12,4	2,01E-5	3,23E-6	16,1	6,24E+1	1,19E+1	19,1
447,3	404,9	12,1	1,27E-5	2,17E-6	17,1	4,27E+1	8,57E+0	20,1
437,2	395,5	11,9	1,08E-5	1,79E-6	16,7	3,94E+1	7,79E+0	19,8
427,1	386,0	11,6	6,69E-6	1,18E-6	17,6	2,67E+1	5,52E+0	20,7
417,1	376,5	11,3	5,85E-6	9,25E-7	15,8	2,56E+1	4,93E+0	19,3
397,1	357,7	10,7	4,71E-6	8,48E-7	18,0	2,49E+1	5,31E+0	21,4

4. Conclusions

The Laboratory of Analysis by Nuclear Reaction (LARN) at the University of Namur (Belgium) is equipped with a low background γ-ray detection setup, which can be used to perform PIGE analysis, characterization of low-activity nuclear wastes and cross-section measurements.

The main enhancement in comparison with our former system [1] comes from the active shielding, which covers a larger area and makes it possible, in addition to the passive shielding, to mitigate the external background of about one to two orders of magnitude, depending on the energy range under interest.

It is shown that results in direct and reverse kinematics are both in agreement with each other as well as with the literature.

As an important result, we showed that it is possible to study nuclear reactions at very low energy with a single polyvalent detection setup, which can be used either for nuclear reaction measurement, depth-profiling of light elements or for radioactivity analysis. Furthermore, it is possible to measure cross-section over a wide energy range (from 147 to 560 keV), reaching

energies close to the Gamow energy with this single setup. Our low background system reaches the same performances as other facilities generally built for a single application.

To conclude, we showed that it is possible to carry out low background measurements with a relatively low-cost and polyvalent system.

Acknowledgments

The authors would like to acknowledge L. Lambotte for his invaluable help. The authors are grateful to P. Descouvemont for his very useful discussions. This work is supported by the Department of Physics of the University of Namur. This work was achieved with institutional funds in the context of the PhD thesis of P.L. Debarsy and the master thesis of L. Baseil.

Data availability

The data that supports the findings of this study are available within the article.

Bibliography

[1] G. Genard, V.E. Nuttens, V. Bouchat, G. Terwagne, Development of a low-level setup for γ spectroscopy: Application for nuclear astrophysics using reverse kinematics, Nucl. Instruments Methods Phys. Res. Sect. B Beam Interact. with Mater. Atoms. , 268 (2010).
[2] H.A. Bethe, Energy production in Stars, Phys. Rev., 55 (1939) 103.
[3] E.M. Burbidge, G.R. Burbidge, W.A. Fowler, F. Hoyle, Synthesis of the Elements in Stars, Rev. Mod. Phys., 29 (1957) 547-650.
[4] C.E. Rolfs, W.S. Rodney, Cauldrons in the cosmos, 1988.
[5] S. Chakraborty, R. DeBoer, A. Mukherjee, S. Roy, Systematic R-matrix analysis of the 13C(p, γ)14N capture reaction, Phys. Rev. C. , 92 (2015) 045801.
[6] J.D. King, et al., Cross-section and astrophysical S-factor for the 13C(p, γ)14N reaction, Nucl. Phys. A., 567 (1994) 354–376.
[7] R.E. Hester, W.A.S. Lamb, Radiative capture of protons in 13C Phys. Rev. , 121 (2012) 584.
[8] D.F. Hebbard, J.L. Vogl, Elastic scattering and radiative capture of protons by 13C Nucl. Phys., 21 (1960) 652–675.
[9] N.W. Makau, T.E. Derry, A new way of depositing thin targets of monolayer thickness for nuclear reaction analysis: A case of the 550 keV 13C (p,γ)14N resonant nuclear reaction, Detect. Assoc. Equip., 555 (2005) 31–35.
[10] E.J. Woodbury, W.A. Fowler, The Cross-section for the Radiative capture of protons by 13C at 129 keV, Phys. Rev. , 85 (1951) 51.
[11] W. Galster, P. Leleux, I. Licot, E. Lienard, P. Lipnik, D. Mertens, Target and detection techniques for the 13N(p, gamma)14O reaction using radioactive ion beams: 13C(p, gamma)14N reaction as a test case, Phys Rev. C., 44 (1991) 2776-2787.
[12] G. Genard, M. Yedji, G.G. Ross, G. Terwagne, Elaboration and characterization of hydrogen standard stable under heavy ion irradiation: Application to nuclear astrophysics, Nucl. Instrum. Methods Phys. Res. B Beam Interact. Mater. Atoms. , 264 (2007) 156-164.
[13] P.L. Debarsy, G. Terwagne, Pure hydrogen references synthesized by low energy ion implantation into amorphous silicon, Nucl. Instrum. Methods Phys. Res. B, 442 (2019) 47-52.

[14] P.P. Povinec, J.F. Comanducci, I. Levy-Palomo, IAEA-MEL's underground counting laboratory in Monaco - Background characteristics of HPGe detectors with anti-cosmic shielding, Appl. Radiat. Isot. , 61 (2004) 85–93.
[15] H. Gastrich, et al., The Dortmund Low Background Facility - Low-background γ ray spectrometry with an artificial overburden Appl. Radiat. Isot., 112 (2016) 165–176.
[16] L.R. Greenwood, et al., Low-background γ-ray spectrometry for the international monitoring system, Appl. Radiat. Isot., 126 (2017) 240–242.
[17] B. Pérot, et al., The characterization of radioactive waste: a critical review of techniques implemented or under development at CEA, France, EPJ Nuclear Sci. Technol., 4 (2018).
[18] J.I. Byun, H.Y. Hwang, J.Y. Yun, A low background γ-ray spectrometer with a large well, Appl. Radiat. Isot., 156 (2020) 108932.
[19] N.Q. Hung, V.H. Hai, T.K. Tuyet, H.L. Tuan, A Low Background γ Ray Spectrometer with Anticosmic Shielding, Commun. Phys., 26 (2016).
[20] A. Vismes, R. Gurriaran, X. Cagnat, Anti-Compton γ spectrometry for environmental samples, Radioprotection, 44 (2009) 613–618.
[21] R. Longland, C. Iliadis, A.E. Champagne, C. Fox, J.R. Newton, Nuclear astrophysics studies at the LENA facility: The γ-ray detection system, Nucl. Instruments Methods Phys. Res. Sect. A: Accel. Spectrom. Detect. Assoc. Equip., 566 (2006) 452–464.
[22] G.F.C.e.a.f.t.L. collaboration, Direct Measurement of the 13C(α,n)16O Cross-section into the s-Process Gamow Peak, Phys. Rev. Lett. , 127 (2021) 152701
[23] G. Amsel, E. D'Artemare, G. Battistig, E. Girard, L.G. Gosset, P. Révész, Narrow nuclear resonance position or cross-section shape measurements with a high precision computer controlled beam energy scanning system, Nucl. Inst. Methods Phys. Res. B. , 136-138 (1998) 545–550.
[24] D.E. Groom, N.V. Mokhov, S.I. Striganov, Muon stopping power and range tables 10 MeV-100 TeV, At. Data Nucl. Data Tables, 78 (2001) 183–356.
[25] G. Heusser, Low-radioactivity background techniques Annu. Rev. Nucl. Part. Sci. , 45 (1995) 543-590.
[26] A. Guglielmetti, Nuclear astrophysics and underground accelerators, Phys. Dark Universe, 4 (2014) 10-13.
[27] F. Ferraro, G.F. Ciani, A. Boeltzig, F. Cavanna, S. Zavatarelli, The Study of Key Reactions Shaping the Post-Main Sequence Evolution of Massive Stars in Underground Facilities, Front. Astron. Space Sci. , 7 (2021).
[28] J. Skowronski, et al., Advances in radiative capture studies at LUNA with a segmented BGO detector, J. Phys. G: Nucl. Part. Phys., 50 (2023) 045201.
[29] D. Rapagnani, J. Skowronski, A. Boeltzig, Study of proton capture on carbon-13 isotope at LUNA, J. Phys.: Conf. Ser. , 2586 (2023) 012103.
[30] L.B. Bezrukov, et al., New Low-Background Laboratory in the Pyhäsalmi Mine, Finland, Phys. Part. Nucl., 49 (2018) 769–773.
[31] A.C. Dombos, et al., Measurement of Low-Energy Resonance Strengths in the 18O(α,γ)22N reaction, Phys. Rev. Lett., 128 (2022) 162701.
[32] W. Liu, et al., Commissioning of Underground Nuclear Astrophysics Experiment JUNA in China, EPJ Web of Conferences, 260 (2022) 08001
[33] C.S. Reingold, et al., High Efficiency Total Absorption Spectrometer HECTOR for capture reaction measurements, Eur. Phys. J. A, 55 (2019) 77.
[34] C. Nitsch, M. Gerhardt, C. Gößling, K. Kröninger, Improvements to the muon veto of the Dortmund Low Background Facility, Appl. Radiat. Isot. , 126 (2017) 201-203.
[35] Q. Hu, et al., Design of cosmic veto shielding for HPGe-detector spectrometer, Appl. Radiat. Isot., 109 (2016) 474–478.
[36] D.V. Kasperovych, F.A. Danevich, V.V. Kobychev, B.N. Kropivyansky, N.V. Sokur, A.I. Tymoshenko, Low background scintillation setup to investigate radiopurity of materials, Probl. At. Sci., 113 24-31.

[37] R.L. Brodzinski, H.S. Miley, L.H. Reeves, F.T.A. III, Low-background germanium spectrometry: The bottom line, J. Radioanal. Nucl. Chem., 160 (1992) 355–362.
[38] H. Paradis, A.d.V. Ott, X. Cagnat, F. Piquemal, R. Gurriaran, Leda: A γ-γ coincidence spectrometer for the measurement of environment samples, Appl. Radiat. Isot. , 126 (2017) 179-184.
[39] K. von Sturm, et al., A Compton scattering setup for pulse shape discrimination studies in germanium detectors, Appl. Radiat. Isot., 125 (2017) 163-168.
[40] S. Garti, et al., Characterizing low-activity waste containers: A case study for Compton Suppression Systems under challenging signal-to-noise ratio, Nucl. Instrum. Methods Phys. Res. A, 949 (2020) 162806.
[41] R. Britton, Compton suppression systems for environmental radiological analysis, J. Radioanal. Nucl. Chem., 292 (2012) 33-39.
[42] R. Britton, J.L. Burnett, A.V. Davies, P.H. Regan, Monte-Carlo optimisation of a Compton suppression system for use with a broad-energy HPGe detector, Nucl. Instrum. Methods Phys. Res. A 762 (2014) 42-53.
[43] G.F. Knoll, Radiation detection and measurement, 1989.
[44] G. Heusser, M. Wojcik, Radon suppression in low-level counting, Int. J. Radiat. Appl. Instrumentation. A. Appl. Radiat. Isot., 43 (1992) 9–18.
[45] CAEN, DT5724 User Manual, 2017.
[46] H. Damjantschitsch, M. Weiser, G. Heusser, S. Kalbitzer, H. Mannsperger, An in-beam-line low-level system for nuclear reaction γ-rays, Nucl. Instruments Methods Phys. Res. , 218 (1983) 129–140.
[47] J. I. Byun, et al., An anticoincidence-shielded γ-ray spectrometer for analysis of low level environmental radionuclides, Appl. Radiat. Isot. , 58 (2003) 579–583.
[48] J. Vojtyla, A computer simulation of the cosmic-muon background induction in a Ge γ-spectrometer using GEANT, Nucl. Instruments Methods Phys. Res. B 100 (1995) 87-96.
[49] N. Q. Hung, V.H. Hai, M. Nomachi, Investigation of cosmic-ray induced background of Germanium gamma spectrometer using GEANT4 simulation, Appl. Radiat. Isot., 121 (2017) 87-90.
[50] K. Shizuma, K. Fukami, K. Iwatani, H. Hasai, Low-background shielding of Ge detectors for the measurement of residual 152Eu radioactivity induced by neutrons from the Hiroshima atomic bomb, Nucl. Inst. Methods Phys. Res. B. , 66 (1992) 459–464.
[51] J. Laurec, X. Blanchard, F. Pointurier, A. Adam, A new low background γ spectrometer equipped with an anti-cosmic device, Nucl. Instruments Methods Phys. Res. A: Accel. Spectrometers, Detect. Assoc. Equip. , 369 (1996) 566–571.
[52] M. V. Sivers, et al., Low-level γ-ray spectrometry at the underground laboratory Garching, Appl. Radiat. Isot. , 91 (2014) 49–56.
[53] F. Perrot, et al., Evidence of 131I and 134,137Cs activities in Bordeaux, France due to the Fukushima nuclear accident, J. Environ. Radioact., 114 (2012) 61-65.
[54] G. Heusser, et al., GIOVE: a new detector setup for high sensitivity germanium spectroscopy at shallow depth, Eur. Phys. J. C. , 75 (2015) 1-16.
[55] M. Köhler, et al., A new low-level γ-ray spectrometry system for environmental radioactivity at the underground laboratory Felsenkeller, Appl. Radiat. Isot. , 67 (2009) 736–740.
[56] J.L. Reyss, S. Schmidt, F. Legeleux, P. Bonté, Large, low background well-type detectors for measurements of environmental radioactivity, Nucl. Inst. Methods Phys. Res. A. , 357 (1995) 391–397.
[57] S. Turkat, et al., A new ultra low-level HPGe activity counting setup in the Felsenkeller shallow-underground laboratory, Astropart. Phys. , 148 (2023) 102816
[58] G. Genard, P. Descouvemont, G. Terwagne, S-factor measurement of the 13C(p,γ)14N reaction in reverse kinematics, J. Phys. Conf. Ser., 202 (2010).
[59] T.M. Semkow, et al., Low-background γ spectrometry for environmental radioactivity, Appl. Radiat. Isot. , 57 (2002) 213–223.
[60] H.S. Miley, R.L. Brodzinski, J.H. Reeves, LOW-BACKGROUND COUNTING SYSTEMS COMPARED, J. Radioanal. Nucl. Chem., 160 (1992) 371–385.

[61] M. Schwaiger, F. Steger, T. Schroettner, C. Schmitzer, A ultra low level laboratory for nuclear test ban measurements, Appl. Radiat. Isot., 56 (2002) 375–378.
[62] F. Ajzenberg-Selove, Energy levels of light nuclei A = 13-15, Nucl. Phys. A. , 268 (1976) 1-196.
[63] W.A. Lanford, Analysis for hydrogen by nuclear reaction and energy recoil detection, Nucl. Instruments Methods Phys. Res. B. , 66 (1992) 65–82.
[64] S. Agostinelli, et al., GEANT4 - A simulation toolkit, Nucl. Instruments Methods Phys. Res. A, 506 (2003) 250–303.
[65] J.L. Vogl, Radiative capture of protons by 12C and 13C below 700 keV, 1963.
[66] R. Hellborg, M. Kiisk, P. Persson, K. Stenström, Vacuum in an accelerator system - Calculations and measurements, Vacuum., 78 (2005) 427–434.